Systematic design of a multi-input multi-output controller by model-based decoupling

PAPER • OPEN ACCESS

Systematic design of a multi-input multi-output controller by model-based decoupling: a demonstration on TCV using multi-species gas injection

To cite this article: J.T.W. Koenders *et al* 2023 *Nucl. Fusion* **63** 106007

OPEN ACCESS
IOP Publishing | International Atomic Energy Agency
Nuclear Fusion
Nucl. Fusion **63** (2023) 106007 (11pp)
https://doi.org/10.1088/1741-4326/acee0f

Systematic design of a multi-input multi-output controller by model-based decoupling: a demonstration on TCV using multi-species gas injection

J.T.W. Koenders[1,2,*], A. Perek[3], C. Galperti[3], B.P. Duval[3], O. Février[3], C. Theiler[3], M. van Berkel[1] and the TCV Team[a]

[1] DIFFER—Dutch Institute for Fundamental Energy Research, Eindhoven, Netherlands
[2] Department of Mechanical Engineering, Control Systems Technology Group, Eindhoven University of Technology, Eindhoven, Netherlands
[3] École Polytechnique Fédérale de Lausanne (EPFL), Swiss Plasma Center (SPC), Lausanne, Switzerland

E-mail: j.t.w.koenders@differ.nl

Received 12 May 2023, revised 11 July 2023
Accepted for publication 8 August 2023
Published 24 August 2023

Abstract

In this paper, we present the first results of a systematically designed multi-input multi-output gas-injection controller on Tokamak á Configuration Variable (TCV). We demonstrate the simultaneous real-time control of the NII emission front position and line-integrated electron density using nitrogen and deuterium gas injection. Injection of nitrogen and/or deuterium affects both the NII emission front position and line-integrated electron density. This interplay between control loops is termed interaction and, when strongly present, makes designing a controller a significantly more complex problem. Interaction between the control loops can be reduced to an acceptable level by redefining inputs, decoupling the multi-input multi-output control problem to separated single-input single-output problems. We demonstrate how to achieve this by defining virtual control inputs from linear combinations of the actuators available. For the demonstration on TCV, linear combinations of deuterium and nitrogen gas injection are computed from transfer-function models to obtain these virtual inputs. The virtual inputs reduce the interaction in the control-relevant frequency range to a point where control of the NII emission front position and line-integrated electron density can be considered decoupled, allowing for the much simpler design of single-input single-output controllers for each loop. Implementing the controllers with the virtual inputs gives the multi-input multi-output gas-injection controller. This approach is well established in the control community, and is presented here as a demonstration to drive developments of multi-input multi-output control strategies. In particular, the envisioned control of particle- and heat fluxes impacting the divertor targets by injection of multiple gas species.

[a] See Reimerdes *et al* 2022 (https://doi.org/10.1088/1741-4326/ac369b) for the TCV Team.
[*] Author to whom any correspondence should be addressed.

Keywords: TCV, decoupling, exhaust control, MIMO control

(Some figures may appear in colour only in the online journal)

1. Introduction

One of the major challenges identified before tokamak fusion reactors can become viable, is the handling of their heat and particle exhaust [1, 2]. Without mitigation, the expected power fluxes leaving the high-temperature plasma will exceed present-day material engineering limits [3, 4]. The main approach considered to achieve acceptable power fluxes during operation is the injection of several gas species into the tokamak exhaust region [5, 6], called the divertor. Real-time control algorithms that actively assess the exhaust plasma state are required to maintain safe operation, responding to changing core-plasma conditions, disturbances and transient events by adjusting the amount of gas injected.

Active control of the plasma exhaust flux using a single gas species has been performed on many operational tokamaks [7–13]. However, for reactor-relevant mitigation, multiple gas species will need to be injected simultaneously. At the least, two species are required: fueling of reaction isotopes, and seeding of a heavier impurity species to radiate power within the scrape-off layer (SOL). In envisioned demonstration power plants such as DEMO, a significant amount of the fusion power must also be radiated within the confined core, requiring a third gas species to efficiently radiate from the hotter plasma within the last-closed-flux surface [14].

This multiple gas species requirement, where each injected quantity will likely affect the quantity required of the others, makes exhaust control in fusion reactors inherently a multi-input multi-output (MIMO) control problem. Feedback control of radiation and detachment using multiple gas injection actuators has been reported from ASDEX Upgrade [14] and DIII-D [15]. These works treated the two control loops as decoupled, implicitly assuming interference between the loops is negligible and that each used actuator only affects one of the control parameters. In [15] it was recognized interference was present, and it was partially quantified, but was considered negligible and not further used in the controller design. Both works reported that no disruptive interference between the assumed to be separated control loops was observed.

In practice, such MIMO control problems almost always exhibit some interference between the control loops. This interference between control loops is termed *interaction*, and can be methodically quantified and accounted for [16], where the aim is to reduce such interaction at control-relevant frequencies to a level where the control loops may be considered decoupled.

For exhaust control, each injected gas-species will have a complex effect upon the plasma. They will not only affect a single important parameter (such as core- or divertor radiation, or target fluxes) but multiple parameters simultaneously. If interaction is present, but ignored, the performance limit of each individual control loop will be unnecessarily low. Furthermore, strong interaction between control loops deteriorates the validity of robustness and performance margins obtained from model-based controller design on the individual loops, e.g. controllers able to stabilize the individual loops can become unstable when implemented together [16].

In this paper, we describe a method to quantify the interaction between control loops and then significantly reduce it within a control-relevant frequency range. This is achieved by defining new, virtual, control inputs from linear combinations of the available actuators. This simplified form of this method is well imagined by considering the modernization of the faucet, by moving from knobs (actuators) that actuate the total hot- and cold-water flow, to those that actuate flow and temperature separately. This way of combining the available actuators to align their action with the desired control parameters is called decoupling, and can be implemented in a control system programmatically.

A decoupling scheme analogous to the faucet example was implemented in JET to simultaneously control the hydrogen-deuterium ratio and ELM frequency using gas injection actuators [17]. This decoupling scheme was based on steady-state gain data, and showed a significant improvement in the control performance. However, this approach can be improved by decoupling the system at control-relevant frequency range, i.e. the desired bandwidth frequency, as model-based stability and performance margins are defined at this point. When the control bandwidth frequency is significantly higher than zero, it can no longer be guaranteed that the steady-state decoupling scheme presented in [17] remains effective.

We experimentally demonstrate decoupling at a control-relevant frequency range by the systematic design and application of a MIMO gas injection controller for the Tokamak á Configuration Variable (TCV) tokamak. We show the successful real-time control of two output parameters: the NII (399.4 nm) impurity emission front position y_{NII}, used as a measure of detachment progression in TCV [18], and the line-integrated core electron density $y_{\mathrm{n_e}}$, a core-plasma control parameter. These parameters are actuated by injecting deuterium (D_2) and nitrogen (N_2) into the divertor.

This paper is organized as follows. In section 2, we show how to quantify interaction in a MIMO setting using a relative-gain-array (RGA) analysis on an example model. We then show how to combine the available actuators to obtain virtual inputs which reduce the quantified interaction between the control loops. This is done using a pre-compensator, decoupling the controller design problems. In section 3 we apply this approach to a MIMO control problem on TCV. We present the experimental set-up, and estimate a transfer-function model for the system. Using the RGA analysis we show significant interaction is present, and then subsequently reduce it by

developing a pre-compensator. In section 4 we design a controller for each, now decoupled, control problem with the computed virtual inputs. The resulting MIMO controller is experimentally demonstrated on TCV, and is shown to simultaneously control y_{n_e} and y_{NII} within a useful operating space. We conclude in section 5 and discuss the results.

2. The pre-compensator decoupling method

In this section, we use an example model to show how to compute a linear combination of available actuators, termed a pre-compensator, to decouple a MIMO control problem. The reader familiar with this method can proceed directly to section 3.

We consider a multi-input multi-output example system H in the form of coupled linear differential equations

$$\begin{bmatrix} \frac{dy_1}{dt} \\ \frac{dy_2}{dt} \\ \vdots \\ \frac{dy_n}{dt} \end{bmatrix} = A^{n\times n} \begin{bmatrix} y_1 \\ y_2 \\ \vdots \\ y_n \end{bmatrix} + B^{n\times m} \begin{bmatrix} u_1 \\ u_2 \\ \vdots \\ u_m \end{bmatrix}, \tag{1}$$

with the systems inputs (actuators) and outputs (measured quantities) defined as $u_{1..m}$ and $y_{1..n}$, respectively. For the example model we choose $m = n = 2$ and fill in arbitrary numbers for matrices A and B to obtain

$$H: \begin{cases} \frac{dy_1}{dt} = -4y_1 - 3y_2 + 2u_1 + u_2, \\ \frac{dy_2}{dt} = -2y_1 - 3y_2 + 2u_1 + 4u_2. \end{cases} \tag{2}$$

Figure 1 shows the corresponding MIMO control problem, where we aim to control the values of $y_{1,2}$ to the desired references $r_{1,2}$ by manipulating the inputs $u_{1,2}$. To this end, we close the loop using a feedback controller C that determines which input values $u_{1,2}$ are required when receiving the tracking errors $e_{1,2} = r_{1,2} - y_{1,2}$ as

$$\begin{bmatrix} u_1 \\ u_2 \end{bmatrix} = \underbrace{\begin{bmatrix} c_{11}(e_1) & c_{12}(e_2) \\ c_{21}(e_1) & c_{22}(e_2) \end{bmatrix}}_{C}. \tag{3}$$

Here, each term in the C matrix is a controller to be designed. For example, $c_{11}(e_1)$ could be a PI controller $u(t) = K_p e_1(t) + K_i \int^t e_1(t)dt$.

From (2) we observe that each input $u_{1,2}$ affects not only one, but both output time-derivatives $dy_{1,2}/dt$. This cross-coupling of inputs to outputs is termed *interaction*, and when significant, it makes designing the controller C a time-consuming and iterative procedure. Even with a diagonal controller, i.e. $c_{12} = c_{21} = 0$, and relatively simple PI controllers for c_{11} and c_{22}, there remain four free design parameters that each affect both control loops.

In order to identify whether the interaction in the example model is significant, we apply a RGA analysis [16].

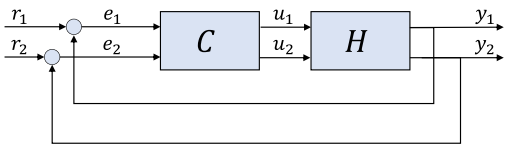

Figure 1. The MIMO process control loop for a 2×2 system H and controller C. Shown signals are the control references r, control errors e, inputs u and outputs y.

2.1. Relative-gain-array

The interaction between the inputs $u_{1,2}$ and outputs $y_{1,2}$ of our model H is quantified by computing its RGA, giving a normalized response magnitude over frequency of each input-output pair. First, we transform our system H to the Laplace domain to obtain a transfer matrix $H(s)$ as

$$\underbrace{\begin{bmatrix} y_1(s) \\ y_2(s) \\ \vdots \\ y_n(s) \end{bmatrix}}_{Y(s)} = H(s)^{n\times m} \underbrace{\begin{bmatrix} u_1(s) \\ u_2(s) \\ \vdots \\ u_m(s) \end{bmatrix}}_{U(s)}, \tag{4}$$

with $s = \sigma + j\omega$ a complex number frequency parameter called the Laplace variable, with real numbers σ and ω. Filling in the numbers of the example model (2) we obtain

$$\underbrace{\begin{bmatrix} y_1(s) \\ y_2(s) \end{bmatrix}}_{Y(s)} = \underbrace{\begin{bmatrix} \frac{2}{s+4} & \frac{1}{s+3} \\ \frac{2}{s+2} & \frac{4}{s+3} \end{bmatrix}}_{H(s)} \underbrace{\begin{bmatrix} u_1(s) \\ u_2(s) \end{bmatrix}}_{U(s)}. \tag{5}$$

The RGA: $= \Lambda(s)$ of the transfer matrix $H(s)$ is then computed from

$$\Lambda(s) = H(s) \circ (H(s)^{-1})^T \tag{6}$$

with $\circ$ indicating an element wise multiplication, or Hadamard product. We can make an insightful plot of $\Lambda(s)$ with a Bode magnitude diagram. Here, $\Lambda(s)$ is evaluated in the Fourier domain $s = j\omega$, interpreted as evaluating the output response of the transfer function to constant amplitude oscillations. The absolute value of $\Lambda(j\omega)$ is then the normalized response magnitude of each input-output pair per frequency $\omega\,(\text{rads}^{-1})$. Figure 2 shows a Bode diagram of $\Lambda(s)$. In a fully decoupled system, only diagonal values will be present, and the off-diagonal terms are zero. As all four magnitudes are in the same order of magnitude for all frequencies, we conclude there is significant interaction between the control loops. This can be alleviated by applying pre-compensator to reduce the RGA values of the off-diagonal terms, effectively diagonalizing the system H, to obtain two decoupled control problems.

2.2. Decoupling with a pre-compensator

Ideally, we would seek to render the RGA response magnitude of the off-diagonal pairs for all frequencies zero, removing the interaction completely. This could be done using the system's

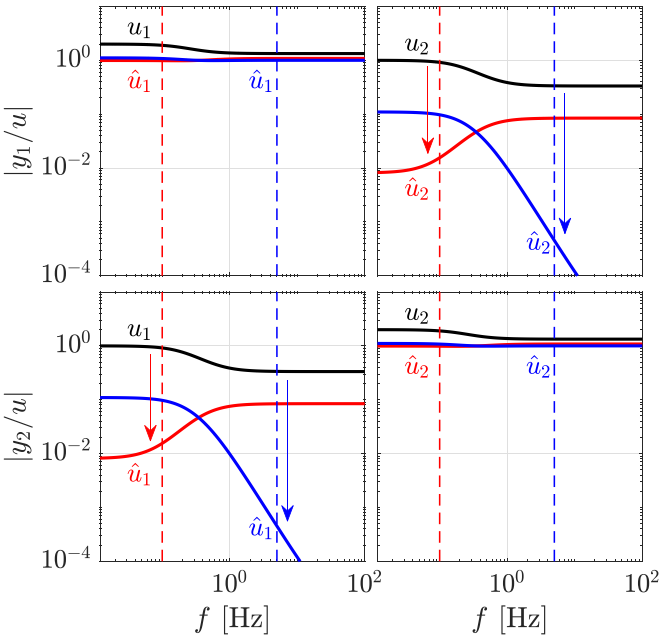

Figure 2. Bode magnitude diagram of the computed RGA $\Lambda(s)$ of the example system $H(s)$ evaluated on $s = j\omega$. Each figure represents the four entries of $\Lambda(s)$, giving the RGA value of the corresponding input u to ouput y. In black, the measure of interaction is shown per frequency without any mitigation. In red a pre-compensator is used to reduce interaction around 0.1 Hz. In blue, a pre-compensator is used to reduce interaction around 5 Hz. The 0.1 Hz and 5 Hz frequencies are indicated by red and blue dashed lines respectively.

inverse to separate the available inputs into a matrix and two virtual inputs $\hat{u}_{1,2}$

$$U(s) = H(s)^{-1}\hat{U}(s), \tag{7}$$

which, would result in

$$Y(s) = \underbrace{H(s)H(s)^{-1}}_{H_{\text{dec}}(s)}\hat{U}(s), \tag{8}$$

having perfect decoupling with respect to the virtual inputs $\hat{u}_{1,2}$, as $H(s)H(s)^{-1}$ becomes the identity matrix for all s and is thus diagonal. However, this is often not possible, in all practical cases, $H(s)^{-1}$ becomes improper and non-causal, i.e. outputs at time t depend on inputs at time $t+\delta$ for some $\delta > 0$.

A solution is to evaluate the inverse of H around a single frequency: $U = H(j\omega)^{-1}\hat{U}$. This frequency is a design parameter, often chosen to be the aimed bandwidth frequency, as this is where the controller its stability margin is defined [16]. Decoupling the system at the bandwidth frequency strongly reduces the probability of inducing instability when implementing multiple, individually stabilizing, controllers simultaneously. As $H(j\omega)^{-1}$ is a complex matrix, we require a real-value approximation for implementation For this we use the ALIGN algorithm $\mathcal{R} : \mathbb{C} \to \mathbb{R}$ [19], which optimally conserves directionality (the phase information) in the least-squares sense. See appendix for the algorithm. The resulting

$$\hat{H}_{\text{inv}}(\omega) = \mathcal{R}(H(j\omega)^{-1}), \tag{9}$$

is called a pre-compensator matrix, that is multiplied with our available actuator vector to obtain the virtual input definitions. The result is a locally (in frequency) decoupled system $H_{\text{dec}}(s) = H(s)\hat{H}_{\text{inv}}$. Choosing, in the example, $\omega = 0$ results in

$$U(s) = \underbrace{H(0)^{-1}}_{\hat{H}_{\text{inv}}(0)}\hat{U}(s) = \begin{bmatrix} 4 & -1 \\ -3 & 1.5 \end{bmatrix}\hat{U}(s). \tag{10}$$

Actuating the system H (5) with the virtual input $\hat{u}_1$ gives $u_1 = 4\hat{u}_1$ and $u_2 = -3\hat{u}_1$, resulting in $y_1 = \hat{u}_1$ and $y_2 = 0$ (for $\omega = 0$), i.e. $\hat{u}_1$ only affect y_1 at the chosen frequency. The same holds for $\hat{u}_2$, resulting in $y_2 = \hat{u}_2$ and $y_1 = 0$ (at $\omega = 0$). Here, the decoupling is perfect (off-diagonal terms are zero) as the matrix $H(0)$ is real, and thus no approximation is required.

Figure 2 shows the result of using a pre-compensator to decouple the problem around two frequencies in the RGA Bode plot. At the chosen frequency, the off-diagonal response amplitude is reduced by more than 2 orders of magnitude. We consider a system where the RGA diagonal terms are at least 2 order of magnitudes higher than the other terms, at the bandwidth frequency, to be decoupled. After decoupling we can design a separate controller for each loop with the newly defined virtual inputs.

Note that, the achievable reduction of interaction depends on the chosen frequency, which may require a design trade-off. This example demonstrates that using a pre-compensator based on the steady-state gain (response at 0 Hz) as in [17] is only effective when the control bandwidth frequency is kept very low. There are methods to decouple the system for larger frequency ranges, for example by using a frequency dependent or state dependent pre-compensator, see [20] and references therein for an overview.

3. Application to TCV

We demonstrate the use of a pre-compensator for a MIMO control problem on the TCV [21]. We choose a 340 kA ohmically heated L-mode discharge in a lower single-null configuration, with reversed field (unfavorable to H-mode access) and $B_{\text{tor}} = 1.4$ T.

3.1. Control problem

As in the model example of section 2 we consider a 2×2 multi-input multi-output control problem. We aim to control the NII (399.5 nm) impurity emission front position and the line-integrated core electron density using simultaneous injection of deuterium (D_2) and nitrogen (N_2) into the divertor region. The NII impurity emission front location is measured using a real-time tracking algorithm [22] upon images acquired from the multi-spectral imaging diagnostic MANTIS [23]. The line-integrated core electron density is measured by a far infrared interferometer (FIR) intersecting the main plasma current centroid. Figure 3 shows the experimental disposition, including the plasma's magnetic equilibrium, gas injection locations and diagnostic views. The MANTIS view of a

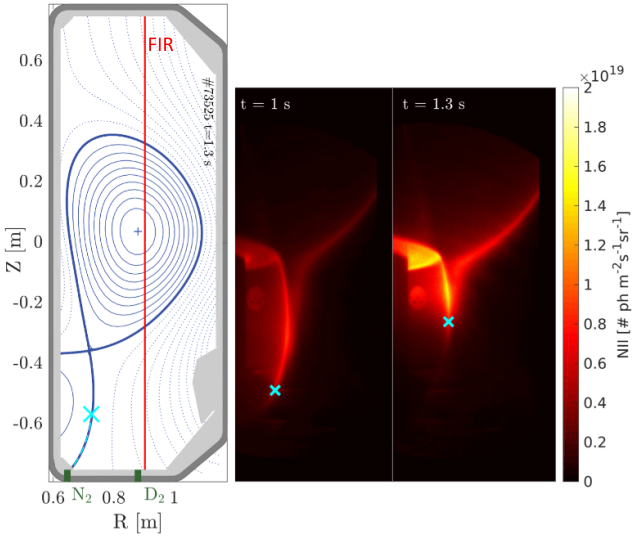

Figure 3. Experimental set-up of the control problem. Left: Poloidal view of TCV with the magnetic equilibrium in blue, gas injection locations in green, FIR line in red and NII-front position definition in cyan. Right: two frames from the MANTIS camera with NII filter. At $t = 1$ s the front position is still close to the target, at $t = 1.3$ s the front position was controlled to $y_{\text{NII}} = 0.2$ m.

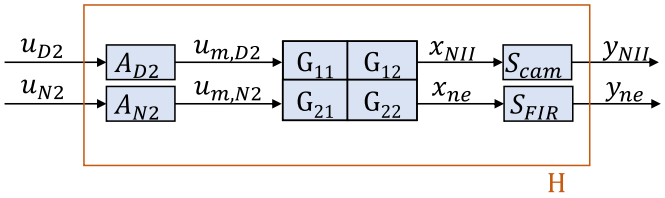

Figure 4. Contents of the TCV control loops represented in a system H, consisting of the gas valve dynamics $A_{\text{D2}}, A_{\text{N2}}$, the 2×2 plasma dynamics G and sensor dynamics $S_{\text{cam}}, S_{\text{FIR}}$.

changing NII front position during a discharge is also shown. The actuators of our control problem are the requested gas injection rates u_{D2} and u_{N2}, which we define as our system inputs. The system outputs are: 1) the front position y_{NII} (m), that is the total distance from the strike point to the point of 50% NII emissivity decrease from the x-point, measured along the divertor leg [22], and 2) the measured line-integrated electron density y_{n_e} (10^{18} m^{-2}). These parameters provide both exhaust- and core-related quantities that would require control in a reactor-like scenario.

We define the dynamics from our inputs u to our outputs y as the system H. A model of the system H is required before we can apply an RGA analysis to quantify the interaction that is present. Figure 4 shows a schematic of the to-be-identified system H consisting of three parts. First, the actuator dynamics $A_{\text{D2,N2}}$ representing the internal gas valve dynamics from requested to actual flow rates. Second, the plant dynamics G, representing the plasma dynamics from injected flow rates to the response of the NII-emission front and the line-integrated electron density. And third, the sensor dynamics S_{cam} and S_{FIR}, which includes filtering, computation times and data transport delays from the MANTIS and FIR sensors respectively. Next,

Table 1. Gas valve model parameters, reproduced from [24]. CC BY 4.0

Parameter	N_2 valve	D_2 valve	Unit
K	0.91	0.97	—
τ	2.00	1.12	ms
τ_d	1.90	1.50	ms

we obtain a transfer-function model estimate of all the eight sub-blocks of H.

3.2. Model estimation

We regress transfer-function models on the system identification results of [24], where identification of the divertor- and core plasma response through y_{NII} and y_{n_e} was measured for both D_2 and N_2 gas injection perturbations. In [24] a transfer-function model from inputs u_{D2} (V) and u_{N2} (V) to output y_{NII} (m) was identified, and is reused here. The dynamics of the valve actuator A, plasma response G and MANTIS diagnostic S were identified separately.

We consider the same gas valves as in [24], and take their identified First-Order Plus Dead-Time actuator models, given in the form of a transfer-function

$$u_m(s) = \underbrace{\frac{K}{\tau s + 1} e^{s\tau_d}}_{A(s)} u(s), \tag{11}$$

with u the requested gas injection rate in Volt, and u_m the measured gas injection rate by an absolutely calibrated pressure transducer at the valve output (also in Volt). Note that, we use here the Volt unit as it is the flow request for the valve actuators. The model parameters K (-), τ (s) and τ_d (s) describe the gain, time constant and delay, respectively. The identified model parameters for both valves are given in table 1.

A dynamic model for S_{cam} was also identified in [24], describing the dynamics from the time-stamp taken halfway through the exposure time of a MANTIS video frame, to the value for a corresponding computed NII front position received by the control system, i.e. the dynamics from x_{NII} to y_{NII} in figure 4. These sensor dynamics are well captured by a delay of 4 ms described by the transfer function

$$y_{\text{NII}}(s) = \underbrace{e^{-0.004\,\text{s}}}_{S_{\text{cam}}} x_{\text{NII}}(s). \tag{12}$$

The FIR system can be described similarly, i.e. using a time-delay between the value measured by the analog electronics, to that received by the controller after processing by a fringe jump compensator algorithm. The dynamics are also well captured by a delay of 4 ms

$$y_{n_e}(s) = \underbrace{e^{-0.004\,\text{s}}}_{S_{\text{FIR}}} x_{n_e}(s). \tag{13}$$

With these dynamic models for the actuators and sensors, we come to the more involved identification of the plasma response dynamics $G(s)$, partitioned as

Table 2. x_{NII} response model parameters.

Parameter	G_{11}	G_{12}	Unit
D	4.424	17.136	$\mathrm{m^2\,s^{-1}}$
$\hat{x}$	0.249	0.054	m
L	0.427	2.625	m

Table 3. x_{n_e} response model parameters.

Parameter	G_{21}	G_{22}	Unit
D	4.424	17.136	$\mathrm{m^2\,s^{-1}}$
$\hat{x}$	0.249	0.054	m
L	0.427	2.625	m

$$\underbrace{\begin{bmatrix} x_{\mathrm{NII}}(s) \\ x_{\mathrm{n_e}}(s) \end{bmatrix}}_{X(s)} = \underbrace{\begin{bmatrix} G_{11}(s) & G_{12}(s) \\ G_{21}(s) & G_{22}(s) \end{bmatrix}}_{G(s)} \underbrace{\begin{bmatrix} u_{m,D2}(s) \\ u_{m,N2}(s) \end{bmatrix}}_{U_m(s)}. \tag{14}$$

In [24], the local models G_{11} and G_{12} were identified using system identification experiments. We use the term *local* as these transfer function models are linear approximations of the dynamics, and only consider these models valid within a region of operational space around the experimental measurements. A diffusion-based transfer-function model, which can describe the locally measured dynamics [25], was regressed on the experimental dynamic measurements obtained by system identification. The system identification method was a perturbation on the inputs using multi-sinusoidals, which result in multi-sinusoidals of equal frequency on the outputs with a change in amplitude and phase shift, giving a data point for each used frequency on a Bode diagram. More information on this method, and these measurements, can be found in [12, 24–26].

The model structure for regression was

$$x_{\mathrm{NII}}(s) = \frac{\cosh(\hat{x}\lambda)\tanh(L\lambda) - \sinh(\hat{x}\lambda)}{D\lambda} u_m(s), \tag{15}$$

where $\hat{x}$, L and D represent the evaluation location, domain size, and diffusion coefficient, respectively, and $\lambda = \sqrt{s/D}$ with s the Laplace complex frequency variable as introduced in section 2. Table 2 presents the identified parameters.

During the system identification experiments of [24], the response of the line-integrated electron density was measured, but not further investigated. We revisit that measured response data to identify the transfer-function models from inputs u_{D2} (V) and u_{N2} (V) to output y_{n_e} ($10^{18}\,\mathrm{m^{-2}}$), i.e. identifying G_{21} and G_{22}. We take the same approach as in [24], and assume a similar transfer-function structure to regress upon the response data of the line-integrated density

$$x_{n_e}(s) = \frac{\cosh(\hat{x}\lambda)\tanh(L\lambda) - \sinh(\hat{x}\lambda)}{D\lambda} u_m(s). \tag{16}$$

The frequencies at which a response can be measured using sinusoidal perturbations is lower limited by the experimental discharge duration. Therefore, an estimate of the response on the zero-frequency (DC-gain), i.e. $s = 0$, is required to obtain a unique regression of D, L and $\hat{x}$ [25]. We have obtained an estimate of this steady-state gain by analyzing previous experiments with D_2 fueling and N_2 seeding in the chosen scenario. In similar flat top conditions, we find an increase of 1 V in D_2 fueling request signal converges to an increase of $8.5 \cdot 10^{18}\,\mathrm{m^{-2}}$ in line-integrated density, corresponding to $G_{21}(0) = 8.5$. An increase of 1 V in N_2 seeding converges to a decrease of $0.91 \cdot 10^{18}\,\mathrm{m^{-2}}$ in the line-integrated density, corresponding to $G_{22}(0) = -0.91$. For more information on the DC-gain and its relevance in regressing this transfer-function model, refer to [25]. The transfer-function parameters $\hat{x}$, L and D are regressed on the system identification measurements and estimated steady-state gains by minimizing a least-squares cost function in the complex plane. Table 3 presents the identified parameters for the line-integrated electron density response transfer-function models G_{21} and G_{22}.

The models for actuators A, plant G and sensors S can now be combined to construct the transfer-function matrix for the system $H(s)$ as

$$\begin{bmatrix} H_{11}(s) & H_{12}(s) \\ H_{21}(s) & H_{22}(s) \end{bmatrix} = \begin{bmatrix} A_{D2}(s)G_{11}(s)S_{\mathrm{cam}}(s) & A_{N2}(s)G_{12}(s)S_{\mathrm{cam}}(s) \\ A_{D2}(s)G_{21}(s)S_{\mathrm{FIR}}(s) & A_{N2}(s)G_{22}(s)S_{\mathrm{FIR}}(s) \end{bmatrix}. \tag{17}$$

As in [25], we validate the obtained models with experimental data by comparing the model to the full measured response from inputs $u_{\mathrm{D2,N2}}$ to the outputs $y_{\mathrm{NII},ne}$, that is including the dynamics of the gas injection actuators and FIR and MANTIS sensors. Figure 5 shows a Bode diagram of the model $H(s)$, corresponding system identification measurements M and estimated steady-state gain. Note that, for the response of y_{ne} to u_{N2} (H_{22}), there are only two data-points rather than the four data-points available for the other three responses. This is due to low signal-to-noise ratio in the corresponding higher frequency measurements, as the magnitude response of y_{ne} is significantly lower ($\approx 10\times$) for N_2 than for D_2. Additionally, a phase difference of 180° between H_{21} and H_{22} results from the line-integrated electron density y_{ne} responding positively to D_2, but negatively to N_2. This is likely caused by a reduction in ionization reaction rate following N_2 injection [18].

As shown, the identified model $H(s)$ describes the measured frequency response data well; therefore we can now analyze the interaction in our system H by an RGA analysis.

3.3. Interaction: analysis and mitigation

The RGA $\Lambda(s)$ of $H(s)$ is computed using (6). A bode magnitude plot of the result is depicted in figure 6. Black lines indicate the normalized response magnitude per frequency for the two gas-injection inputs to the line-integrated density and NII front position. Both u_{D2} and u_{N2} affect both outputs y_{n_e} and y_{NII} with RGA values between 0.3 and 1. Note that, in the original system (not decoupled), the strongest response is in the off-diagonal input-output pairs, indicating u_{N2} dominantly affects y_{NII}, and u_{D2} dominantly affects $y_{\mathrm{n_e}}$, as may be

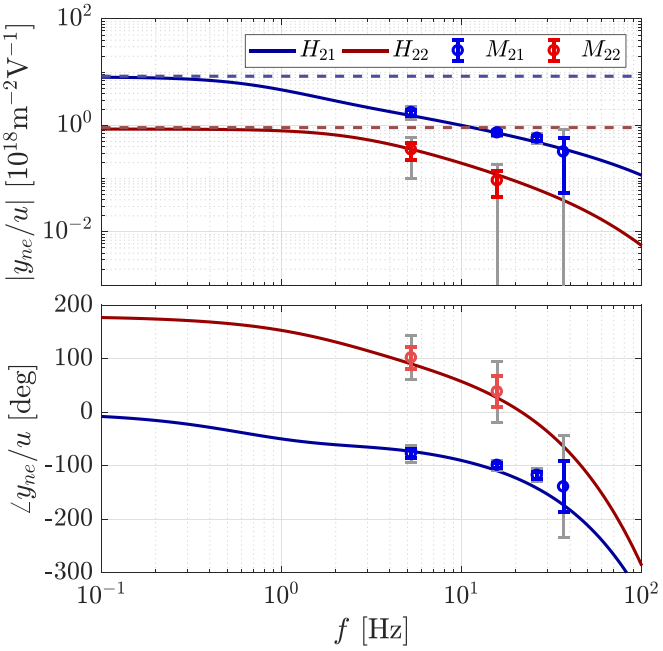

Figure 5. Bode plot of the transfer-function models $H_{21}(s)$ and $H_{22}(s)$ on FRF measurements M_{21} and M_{22}, for the response of y_{n_e} to u_{D2} and u_{N2} respectively. The dashed lines are the estimated DC-gains $H_{21}(0)$ and $H_{22}(0)$, i.e. including valve and sensor models. Measurements are shown with 1σ and 2σ errorbars, in colored and gray, respectively.

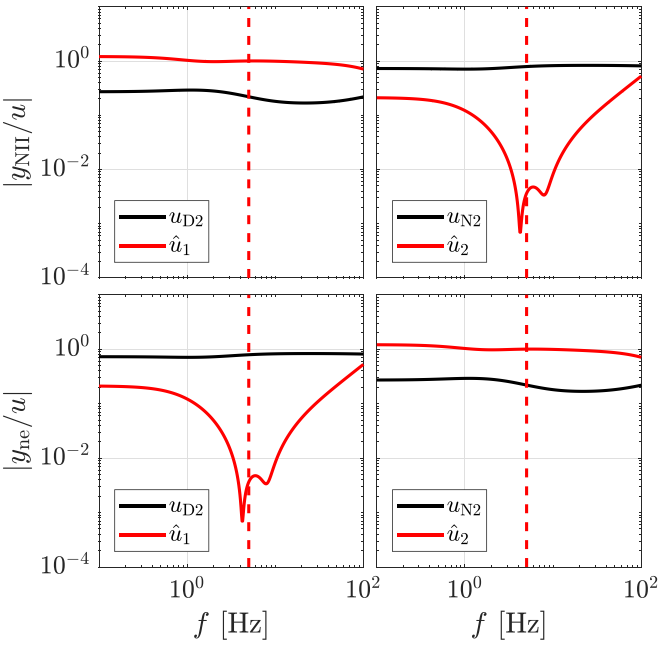

Figure 6. Bode magnitude diagram of the computed RGA for the system $H(s)$, with and without the pre-compensator $\hat{H}_{\text{inv}}$, shown in red, and black respectively. The dashed red-line indicates the chosen decoupling frequency $f = 5$ Hz.

expected. This is caused by the choice of ordering of inputs and outputs and does not affect the result after decoupling.

As the off-diagonal values are of an equal order of magnitude as the diagonal terms, the system is far from decoupled. We aim to reduce the values on the off-diagonal terms by using a pre-compensator as described in section 2, to decouple the control loops and then design a controller for each loop individually.

The pre-compensator is computed using the inverse of the identified transfer-function matrix at the envisioned controller bandwidth. We aim to design a controller that obtains a 5 Hz bandwidth for both control loops, so that y_{NII} and y_{n_e} are controlled with approximately equal performance. The 5 Hz bandwidth is chosen as a slightly more conservative design goal than the 7 Hz bandwidth controller used for the SISO control of the NII emission front position in [24], yet still provides sufficient performance for the control demonstration.

To compute the pre-compensator we follow the steps shown in section 2, repeated here for convenience. We first obtain the inverse of the identified transfer-function matrix at 5 Hz

$$H(j\omega)|^{-1}_{\omega=5\cdot 2\pi} = \begin{bmatrix} 0.027 - 0.031i & 0.030 - 0.019i \\ 0.045 - 0.144i & -0.008 + 0.036i \end{bmatrix}. \quad (18)$$

Then use the ALIGN algorithm to obtain the normalized real-valued approximation

$$\hat{H}_{\text{inv}} = \begin{bmatrix} 0.24 & 0.89 \\ 1 & -1 \end{bmatrix}, \quad (19)$$

and finally use $\hat{H}_{\text{inv}}$ to define new virtual inputs which relate to our gas injection requests as

$$\begin{bmatrix} u_{\text{D2}} \\ u_{\text{N2}} \end{bmatrix} = \hat{H}_{\text{inv}} U^*(s) = \begin{bmatrix} 0.24\hat{u}_1 + 0.89\hat{u}_2 \\ \hat{u}_1 - \hat{u}_2 \end{bmatrix}. \quad (20)$$

Applying the virtual inputs to our system results in a new RGA that significantly reduces the off-diagonal values around the envisioned bandwidth of 5 Hz by more than two orders of magnitude with respect to the diagonal terms. Figure 6 shows the result in red for comparison to the original situation in black. The virtual inputs $\hat{u}_1$ and $\hat{u}_2$ result in a dominant response of y_{NII} and y_{n_e} respectively, decoupling the system around the envisioned bandwidth frequency. A physical interpretation of these virtual inputs can be described as follows. When actuating $\hat{u}_1$ we inject a ratio of $\frac{0.24}{1}\ \frac{D_2}{N_2}$, that both positively affect the position of the front y_{NII}. Meanwhile the negative effect of the added nitrogen upon the line-integrated density is compensated by the right amount of additional deuterium. When actuating $\hat{u}_2$ we inject a ratio of $\frac{0.89}{-1}\ \frac{D_2}{N_2}$, which keeps the front position approximately steady but changes line-integrated density. This is achieved by injecting u_{D2} to increase fueling while significantly reducing u_{N2} injection to compensate for the increased neutral pressure in the divertor by reducing the nitrogen concentration.

The new inputs result in close to diagonal RGA values at the aimed 5 Hz bandwidth for both control loops. We can now design a controller for each loop separately using the obtained virtual inputs.

Table 4. Controller design parameters K_p and K_i with resulting bandwidths and phase margins.

	$C_{NII}(s)$	$C_{n_e}(s)$	Unit
K_p	11	4	—
K_i	20π	12π	rad s^{-1}
Bandwidth	5	5	Hz
Phase margin	72	50	deg.

4. MIMO controller design and demonstration

4.1. Controller design

The MIMO controller design is reduced to two SISO controllers that compute the required virtual input values $\hat{u}_1$ and $\hat{u}_2$ from the tracking errors e_{NII} and e_{n_e}, respectively. The Controllers are designed using the loop-shaping method [16]. Here, the open-loop transfer-function $L(s) = H(s)\hat{H}_{inv}C(s)$ is *shaped* towards performance and stability margins set by the user. These are generally taken as the bandwidth (performance) and phase margin (stability margin). Generally speaking, the higher the bandwidth, the lower the phase margin, with a smaller margin for modeling errors in $H(s)$, i.e. a robustness/performance trade-off. The interested reader can find more information in [27, 28] on the corresponding control theory and in [29] for a detailed example of its use in fusion research. Generally a minimum of 30° phase margin is used as a rule-of-thumb for performance focused design. We set our design goals at a bandwidth of 5 Hz and a phase margin of 50° to stay robust to modeling errors.

We design two PI controllers of the form

$$C(s) = K_p \frac{s + K_i}{s}, \tag{21}$$

where the controller gains K_p and integrator cut-off frequencies K_i are chosen to obtain our design goals of bandwidth and phase margin. Resonances in this system are not expected as its dynamics are (gas) transport driven, therefore we refrain from using a derivative term within the controller, i.e. not a PID. A 40 Hz IIR low-pass filter [30] is added to C_{NII} to reduce higher-frequency measurement noise in y_{NII} originating from sawtooth crashes [24]. The controllers are implemented using the clamping anti-windup method, that saturates the integral action build-up above a pre-defined value, preventing overshoot caused by long rise times [31]. Table 4 shows the resulting controller parameters.

We verify that the designed bandwidth and phase margin of the individual SISO loops may be taken as representative of their application on the MIMO system by using the generalized Nyquist criterion. In the interest of brevity, the interested reader is referred to [27, 32] for details on the Nyquist stability criterion. We highlight the key result here by analyzing a Nyquist diagram, depicting the SISO open-loop gain $L(s) = H(s)C(s)$ evaluated at $s = j\omega$ for $-\infty \leqslant \omega \leqslant \infty$ in the complex plane. The phase margin (stability margin) of a SISO control loop is obtained by taking the total phase rotation from the 'point of instability', located at $(-1,0)$, to the point where the loop gain $|L(j\omega)| = 1$. The value for ω where $|L(j\omega)| = 1$ is the bandwidth frequency. We evaluate the phase margin for the two diagonal loops of the decoupled system, as well as for the full system including the off-diagonal terms. To include the interaction (off-diagonal terms) of the full system, we evaluate the eigenvalues $\lambda_{1,2}(j\omega)$ of the matrix $L(j\omega)$, known as characteristic loci. These Loci generalize the notion of a stability margin of a SISO system in a MIMO-relevant way. When decoupling is done correctly, the phase margins of $\lambda_{1,2}(j\omega)$ and the individual loops L_{11}, L_{22} should be approximately equal, indicating the obtained model-based phase margins are maintained when implementing the controllers simultaneously. Figure 7 shows both the phase margins of the full system, and the individual diagonal loops in a *Nyquist diagram*.

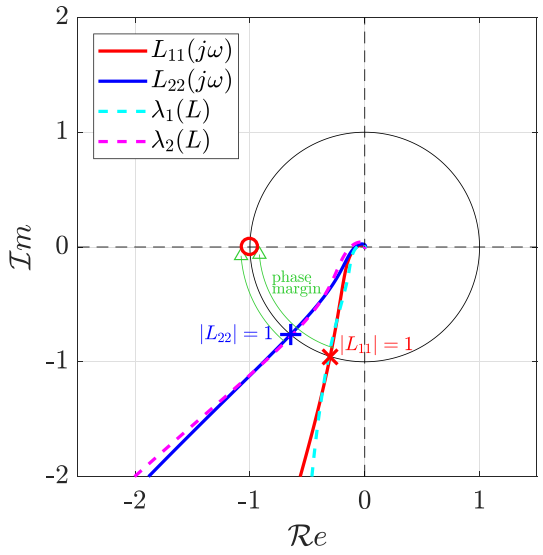

Figure 7. Nyquist diagram showing the loop-gains $L(j\omega)$ plotted in the complex plane. The 'point of instability' is indicated by the red circle. L_{11} and L_{22} represent only the diagonal terms, i.e. the loops using the virtual inputs $\hat{u}_{1,2}$ assuming all interaction is removed. The characteristic loci $\lambda_{1,2}(L)$, or eigenvalues, of the full system include the interaction that is still present after decoupling the system using the virtual inputs. The green arrows show the phase margins visually: the total phase rotation from $|L| = 1$ to the point of instability.

The effect of reducing the interaction by the pre-compensator is observed by a minimal difference in phase margin between the full loop gain L and the diagonal loops gains L_{11} and L_{22} at the bandwidth frequency. Our designed bandwidth and phase margin of the individual SISO loops may thus be taken as representative of their application on the MIMO system with pre-compensator. The MIMO gas-injection controller is now a combination of the pre-compensator and the two SISO controllers. Next, we demonstrate the working of this MIMO gas-injection controller experimentally.

4.2. Experimental demonstration

Figure 8 shows two experimental TCV discharges where the NII emission front position (y_{NII}) and the line-integrated

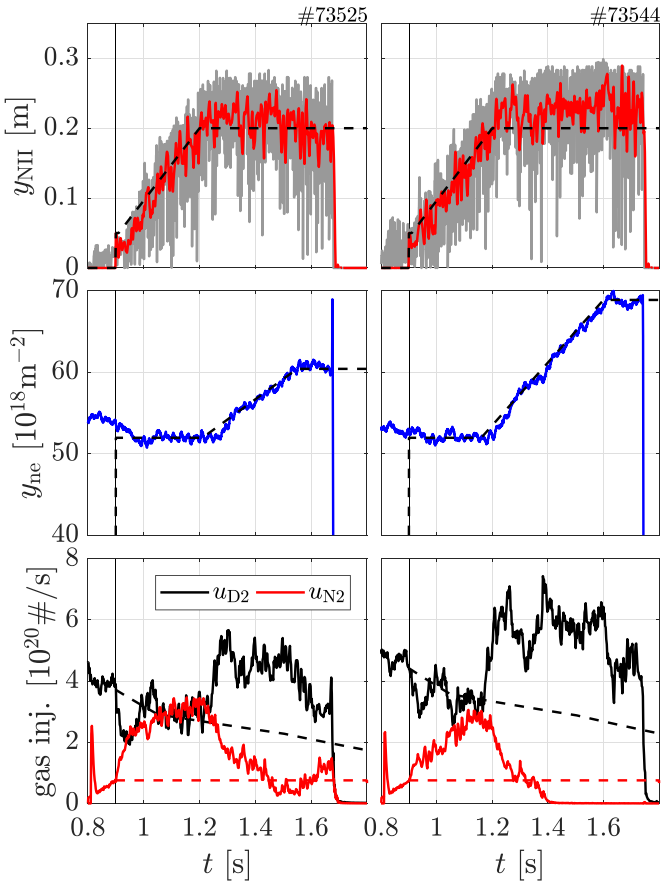

Figure 8. Experimental results for two control experiments, the controller is engaged at $t = 0.9$ s (grey vertical line). Row 1: front position request r_{NII} in dashed black, measured and low-pass filtered front position y_{NII} in gray and red respectively. Row 2: line-integrated density request r_{n_e} in dashed black and measured line-integrated density y_{n_e} in blue. Row 3: total N_2 and D_2 flow rates (full) and pre-programmed feed-forward traces (dashed).

electron density $y_{\mathrm{n_e}}$ were controlled using the same designed MIMO gas-injection controller. In both discharges, the controller is activated at $t = 0.9$ s, its output is summed with a pre-programmed (feed-forward) gas trace for D_2 and N_2. First, y_{NII} is requested to increase to 0.2 m above the divertor target, about halfway between the target and the x-point, while $y_{\mathrm{n_e}}$ is requested constant. Then, the $y_{\mathrm{n_e}}$ request is ramped while maintaining $y_{\mathrm{NII}} = 0.2$ m. In discharge #73525, the controller tracks the two requested references well. However, the requested references can not be chosen arbitrarily as some combinations will hit physics limits, e.g. a too high line-integrated density request will always result in an increase of y_{NII}, even when $y_{\mathrm{NII}} = 0$ is requested. This is demonstrated in discharge #73544. At $t = 1.4$ s the controller ceased the N_2 injection completely, trying to maintain $y_{\mathrm{NII}} = 0.2$ m while increasing y_{n_e}, as requested. Here the controller reaches a physical limit, no negative values of gas injection are possible (no pumping actuator) so y_{NII} cannot descend to its requested reference of 0.2 m. An available pumping actuator may increase the operational space, but may reach other limits, e.g. the impurity concentration cannot be negative. These concerns directly indicate the next development step: using model predictive control strategies or reference governors [33] to account for the physical limits within the system, be it actuator limits, diagnostic limits or the plasma state itself.

5. Conclusion and discussion

The requirement for multiple gas species makes the exhaust control in fusion reactors inherently a MIMO control problem. MIMO control problems require controller design methods that quantify, and if needed, reduce, interaction between the control loops. In this work, we have demonstrated the established local decoupling method of designing a pre-compensator for the MIMO gas-injection control problem on TCV.

We demonstrated the simultaneous real-time control of the NII emission front position and line-integrated electron density using nitrogen and deuterium gas injection actuators. We quantified the interaction between the two control loops using a RGA analysis on an estimated transfer-function model of the system. The initially identified interaction is severely reduced at the chosen bandwidth frequency of 5 Hz by decoupling the system with a pre-compensator. This resulted in a reduction of the off-diagonal RGA values by more than two orders of magnitude than the diagonal terms, effectively decoupling the control problem. A standard controller design technique Loop Shaping was then used to design PI controllers for each, now decoupled, control loop. The final MIMO gas-injection controller is the combination of these two PI controllers and the pre-compensator. This controller was experimentally demonstrated to track combinations of NII emission front position and line-integrated density reference traces. The MIMO controller can be exploited to further explore this operational space systematically through experiments. This allows for an efficient mapping of the operation space spanned by line-integrated electron density and emission front position, rather than an empirical iteration over combinations of feed-forward gas injection traces. The combination of viable references, and thus the operational space spanned by these two control parameters, is inevitably still subject to physical limits. Certain request combinations, for example a high line-integrated electron density and the NII emission front position still at the target, are not physically attainable. Nevertheless, such operational limits can now be identified and related to modelling efforts more efficiently using this controller.

The used static decoupling method is well established in the control community, is extendable to systems with more than two actuators m and sensors n, can readily deal with over-sensing ($m < n$) or over-actuating ($m > n$). Moreover, it can be made dynamic by making the pre-compensator a strictly proper (causal) transfer-function which approximates the system its inverse for a relevant frequency range [16, 20]. This demonstration should drive further development of the required multi-input multi-output gas injection control strategies for future fusion reactors. In particular, a systematic way to attain the envisioned control of the particle and

heat exhaust using combinations of fueling and impurity gas injection appears more accessible.

Acknowledgments

DIFFER is part of the institutes organization of NWO.

This work has been carried out within the framework of the EUROfusion Consortium, partially funded by the European Union via the Euratom Research and Training Programme (Grant Agreement No. 101052200—EUROfusion). The Swiss contribution to this work has been funded by the Swiss State Secretariat for Education, Research and Innovation (SERI). Views and opinions expressed are however those of the author(s) only and do not necessarily reflect those of the European Union, the European Commission or SERI. Neither the European Union nor the European Commission nor SERI can be held responsible for them.

Appendix. ALIGN algorithm

The ALIGN algorithm, which we defined for this work as a function $\mathcal{R}:\mathbb{C}\rightarrow\mathbb{R}$ [19] is a real matrix approximation of a complex matrix. It maintains an optimal directionality conservation in the least-squares sense. The full derivation of the computation can be found in [19], but we repeat the result here for convenience. For a complex matrix, $W^{n\times n}\in\mathbb{C}$ the real-valued approximation $A^{n\times n}\in\mathbb{R}$ is obtained using

$$\begin{aligned} V &= \mathrm{real}(W^{*}W)^{+} \\ Q &= \exp\left(\frac{1}{2}j\angle(\mathrm{diag}(WVW^{T}))\right) \\ A &= (V\cdot\mathrm{real}(W^{*}+\mathrm{diag}(Q)))^{+}, \end{aligned} \tag{A.1}$$

where $^{+}$ indicates a Penrose inverse, * indicates a complex conjugate, and j is the unit imaginary number. The operation *real()* indicates taking only the real values, and *diag()* indicates taking the diagonal matrix values and putting them in a column-vector.

ORCID iDs

J.T.W. Koenders https://orcid.org/0000-0003-4385-923X
A. Perek https://orcid.org/0000-0002-4117-0298
O. Février https://orcid.org/0000-0002-9290-7413
C. Theiler https://orcid.org/0000-0003-3926-1374
M. van Berkel https://orcid.org/0000-0001-6574-3823

References

[1] Donné T. 2018 *European Research Roadmap to the Realisation of Fusion Energy* (EUROfusion)
[2] Zohm H. *et al* 2013 On the physics guidelines for a tokamak DEMO *Nucl. Fusion* **53** 073019
[3] Lipschultz B., LaBombard B., Terry J.L., Boswell C. and Hutchinson I.H. 2007 Divertor physics research on alcator C-Mod *Fusion Sci. Technol.* **51** 369–89
[4] Pitts R.A. *et al* 2019 Physics basis for the first ITER tungsten divertor *Nucl. Mater. Energy* **20** 100696
[5] Loarte A. *et al* (The ITPA Scrape-off Layer and Divertor Physics Topical Group) 2007 Chapter 4: power and particle control *Nucl. Fusion* **47** S203–63
[6] Kallenbach A. *et al* 2013 Impurity seeding for tokamak power exhaust: from present devices via ITER to DEMO *Plasma Phys. Control. Fusion* **55** 124041
[7] Brunner D., Burke W., Kuang A.Q., LaBombard B., Lipschultz B. and Wolfe S. 2016 Feedback system for divertor impurity seeding based on real-time measurements of surface heat flux in the Alcator C-Mod tokamak *Rev. Sci. Instrum.* **87** 023504
[8] Guillemaut C. *et al* 2017 Real-time control of divertor detachment in H-mode with impurity seeding using Langmuir probe feedback in JET-ITER-like wall *Plasma Phys. Control. Fusion* **59** 045001
[9] Eldon D. *et al* 2017 Controlling marginally detached divertor plasmas *Nucl. Fusion* **57** 066039
[10] Komm M. *et al* 2019 Divertor impurity seeding experiments at the COMPASS tokamak *Nucl. Fusion* **59** 106035
[11] Bernert M. *et al* 2021 X-point radiation, its control and an ELM suppressed radiating regime at the ASDEX Upgrade tokamak *Nucl. Fusion* **61** 024001
[12] Ravensbergen T. *et al* 2021 Real-time feedback control of the impurity emission front in tokamak divertor plasmas *Nat. Commun.* **12** 1105
[13] Wu K. *et al* 2021 The achievement of the $T_{\mathrm{e,div}}$ feedback control by CD 4 seeding on EAST *Plasma Phys. Control. Fusion* **63** 105004
[14] Kallenbach A., Bernert M., Eich T., Fuchs J.C., Giannone L., Herrmann A., Schweinzer J. and Treutterer W. 2012 Optimized tokamak power exhaust with double radiative feedback in ASDEX Upgrade *Nucl. Fusion* **52** 122003
[15] Eldon D., Wang H.Q., Wang L., Ding S., Garofalo A.M., Gong X.Z., McLean A.G., Scotti F., Watkins J.G. and Weisberg D. 2023 Integration of high confinement, high poloidal beta plasma with dual radiated power and detachment controls for divertor protection and ELM suppression *Nucl. Mater. Energy* **34** 101332
[16] Skogestad S. and Postlethwaite I. 2007 *Multivariable Feedback Control: Analysis and Design* 2nd edn (Wiley)
[17] Piron L. *et al* 2021 Progress in preparing real-time control schemes for Deuterium-Tritium operation in JET *Fusion Eng. Des.* **166** 112305
[18] Smolders A. *et al* 2020 Comparison of high density and nitrogen seeded detachment using SOLPS-ITER simulations of the tokamak á configuration variable *Plasma Phys. Control. Fusion* **62** 125006
[19] Edmunds J. and Kouvaritakis B. 1979 Extensions of the frame alignment technique and their use in the characteristic locus design method *Int. J. Control* **29** 787–96
[20] Liu L., Tian S., Xue D., Zhang T., Chen Y. and Zhang S. 2019 A review of industrial MIMO decoupling control *Int. J. Control. Autom. Syst.* **17** 1246–54
[21] Reimerdes H. *et al* 2022 Overview of the TCV tokamak experimental programme *Nucl. Fusion* **62** 042018
[22] Ravensbergen T. *et al* 2020 Development of a real-time algorithm for detection of the divertor detachment radiation front using multi-spectral imaging *Nucl. Fusion* **60** 066017
[23] Perek A. *et al* 2019 MANTIS: a real-time quantitative multispectral imaging system for fusion plasmas *Rev. Sci. Instrum.* **90** 123514
[24] Koenders J., Perek A., Kool B., Février O., Ravensbergen T., Galperti C., Duval B.P., Theiler C. and van Berkel M. 2023 Model-based impurity emission front control using deuterium fueling and nitrogen seeding in TCV *Nucl. Fusion* **63** 026006

[25] Koenders J., Wensing M., Ravensbergen T., Février O., Perek A. and van Berkel M. (The TCV Team and The EUROfusion MST1 Team) 2022 Systematic extraction of a control-oriented model from perturbative experiments and SOLPS-ITER for emission front control in TCV *Nucl. Fusion* **62** 066025

[26] van Berkel M. *et al* 2020 Correcting for non-periodic behaviour in perturbative experiments: application to heat pulse propagation and modulated gas-puff experiments *Plasma Phys. Control. Fusion* **62** 094001

[27] Franklin G.F. *et al* 2019 *Feedback Control of Dynamical Systems* 8th edn (Pearson)

[28] Bruijnen D. *et al* 2006 Optimization aided loop shaping for motion systems *Proc. of the 2006 IEEE Int. Conf. on Control Applications* (*Munich, Germany*, *4–6 October 2006*) (IEEE) pp 255–60

[29] Witvoet G., de Baar M.R., Westerhof E., Steinbuch M. and Doelman N.J. 2011 Systematic design of a sawtooth period feedback controller using a Kadomtsev–Porcelli sawtooth model *Nucl. Fusion* **51** 073024

[30] Sutradhar S.R. *et al* 2017 IIR based digital filter design and performance analysis *2017 2nd Int. Conf. on Telecommunication and Networks (TEL-NET)* (*Noida,India*, *10–11 August 2017*) vol 2018 (IEEE) pp 1–6

[31] Åström K.J. and Hägglund T. 2006 *Advanced PID Control* (ISA—The Instrumentation, Systems and Automation Society)

[32] Nyquist H. 1932 Regeneration theory *Bell Syst. Tech. J.* **11** 126–47

[33] Gilbert E.G. and Ong C.-J. 2011 Constrained linear systems with hard constraints and disturbances: an extended command governor with large domain of attraction *Automatica* **47** 334–40